



# CERN Summer Student Program Report

## Optimization of Yield Measurements and Study of $^{229}\text{Ra}$ Decay

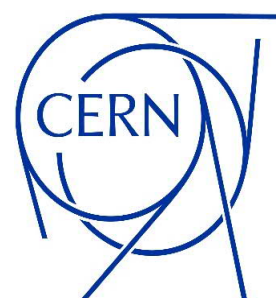
SY-STI-RBS

*Target and Ion Source Development team*

by:

Jakob Birkner Frederiksen

Supervisors: Mia Au  
Line Le  
Date: 30.08.2024



## Abstract

This Summer Student project involved three primary tasks: optimizing the performance of a release curve fitting program, analyzing data from proton scans done using radiation monitors, and analyzing  $^{229}\text{Ra}$  decay to support the development of a nuclear clock.

Firstly, improvements were made to the Release Curve GUI, a tool used for analyzing release curves for yield assessments of isotopes from ISOLDE targets. Enhancements included reactivating database connections for yield comparisons between target setups, preventing crashes, and implementing a numerical integration for fast yield estimation. These updates facilitated more reliable yield calculations.

Secondly, a script was developed to analyze proton scans, which are essential for aligning proton beams with the target material. The script collected and analyzed data from radiation monitors used as an alternative method for conducting a proton scan. Results demonstrated that radiation monitors could potentially replace the tape station for certain tasks, although improvements in real-time data access are necessary.

Finally, the study of  $^{229}\text{Ra}$  focused on identifying and quantifying new gamma lines and their branching ratios. These measurements are crucial for developing a nuclear clock based on the low-energy isomeric transition in  $^{229}\text{Th}$ . The analysis involved energy and efficiency calibration of detectors, fitting decay rates using the Bateman equation, and analyzing gamma spectrums. The results provide insights into  $^{229}\text{Ra}$  decay, contributing to the broader effort to develop ultraprecise timekeeping technologies.

# Contents

<b>1</b>	<b>Release Curves and Yields</b>	<b>1</b>
1.1	Background . . . . .	1
1.2	The Release Curve GUI Program . . . . .	3
1.3	Flaws and User requests . . . . .	3
1.4	Rebuilding the Program . . . . .	4
1.5	Results . . . . .	5
1.6	Further work . . . . .	7
<b>2</b>	<b>Proton Scan</b>	<b>8</b>
2.1	Background . . . . .	8
2.2	The script . . . . .	9
2.2.1	Data . . . . .	9
2.2.2	Analysis . . . . .	10
2.3	Results . . . . .	11
2.4	Further work . . . . .	14
<b>3</b>	<b>Study of <math>^{229}\text{Ra}</math></b>	<b>15</b>
3.1	Background . . . . .	15
3.2	Calibration . . . . .	16
3.3	Analysis and results . . . . .	19
3.3.1	Radioactive molecular beam dataset . . . . .	19
3.3.2	Ion beam dataset . . . . .	20
3.4	Further work . . . . .	22
<b>A</b>	<b>Appendix</b>	<b>23</b>
A.1	Formating of ReleaseCurveGUI.spec . . . . .	23
A.2	Connecting to the spark cluster . . . . .	24
A.3	Finding ratoes of $^{108m}\text{In}$ to $^{108}\text{In}$ . . . . .	25
A.4	splitting overlapping gamma peaks . . . . .	25

# 1 Release Curves and Yields

## 1.1 Background

One of the main goals of the Target and Ion Source Development (TISD) team is to provide targets that can produce the isotopes that the users of the Isotope mass Separator On-Line DEvice (ISOLDE) facility need for their experiments. A crucial value for the users to know is the yield, which is how much of a specific isotope a target can deliver.

At the ISOLDE facility, the process of producing radioactive ion beams from thick target materials involves multiple steps. First, the target material is irradiated by 1.4 GeV proton bunch pulses delivered by the Proton Synchrotron Booster (PBS) [1], producing radioisotopes. The number of isotopes of type  $i$  produced in-target when the protons hit is denoted  $N_{0\ i}$ . The isotopes then have to diffuse and effuse from the target material to the ion source, where they undergo ionization. The ionized atoms are then extracted using an electric field and transported in a beam line using quadrupole magnets leading to an electromagnetic dipole magnet used for mass separation [2]. The amount of extracted and mass-separated ions of a specific isotope is called the yield. It is standard presitue at ISOLDE to divide the yield by the number of protons in each bunch  $N_p$  times the elementary charge  $q$  giving the unit  $[1/C]$ .

Each of the steps in the process, from when the protons hit the target material to when the ions are mass separated, has an associated efficiency. The efficiency of ionization and beam transport to the dipole can be combined into an efficiency  $\varepsilon_f$ . The release efficiency denoted as  $\varepsilon_{release}$ , is dependent on the half-life and is controlled by diffusion and effusion processes. Consequently, it is dependent on the time elapsed between production and release,  $t$ . The probability for a random walking atom to diffuse and effuse to the ion source at a time  $t$  is described by the release density function  $p(t)$  [2]. The release efficiency of an isotope with decay constant  $\lambda$  is obtained by folding the release density function  $p(t)$  with a factor to account for decay losses.

$$\varepsilon_{release} = \int_0^{\infty} p(t) \cdot e^{-\lambda t} dt \quad (1)$$

From these efficiencies and the in-target production of a given isotope  $i$ , a yield can be calculated,  $Y_i$ :

$$Y_i = \frac{N_{0\ i}}{N_p \cdot q} \cdot \varepsilon_f \cdot \varepsilon_{release\ i} = \frac{N_{0\ i}}{N_p \cdot q} \cdot \varepsilon_f \int_0^{\infty} p(t) \cdot e^{-\lambda_i t} dt. \quad (2)$$

Making models of  $p(t)$  from the diffusion and effusion processes results in models that are hard to fit to experimental data. For practical purposes, a simplified fitting approach using a three-exponential function is used:

$$p_i(t, \lambda_r, \lambda_f, \lambda_s, \alpha) = \frac{1}{A}(1 - e^{-\lambda_r t}) \left[ \alpha e^{-\lambda_f t} + (1 - \alpha) e^{-\lambda_s t} \right], \quad (3)$$

$$\text{where,} \quad A = \alpha \left( \frac{1}{\lambda_f} - \frac{1}{\lambda_f + \lambda_r} \right) + (1 - \alpha) \left( \frac{1}{\lambda_s} - \frac{1}{\lambda_s + \lambda_r} \right).$$

$\tau_r = \frac{\ln 2}{\lambda_r}$  describes a sharp rise when the isotope is initially released,  $\tau_f = \frac{\ln 2}{\lambda_f}$  models a fast drop in the released isotope (fast release), whereas  $\tau_s = \frac{\ln 2}{\lambda_s}$  models a slow drop (slow release). An additional parameter  $\alpha$  accounts for the weight between a fast and slow release. These parameters are informative about how isotopes are released and hence how they diffuse, and effuse in the target.

A common yield assessment procedure is based on measuring a release curve. An illustration of how a release curve is measured is shown in Fig. 1 and can be used as a visual representation of the following text describing the same.

The time of proton impact with the target is set to be  $t = 0$ . After a certain delay time,  $t = t_{\text{delay}}$ , deflectors allow the radioactive beam emitted from the target to propagate down the beamline and to the tape of the tape station [3], in which it is implanted for a defined collection time  $t_{\text{collection}}$ . After collection, the beam is again prevented from hitting the tape. The implanted part of the tape is then moved to a measuring position counting the number of  $\beta$  – decays. Taking into account decays during tape transport the rate of ions is found for the time  $t = t_{\text{delay}} + 0.5 \cdot t_{\text{collection}}$ . Iterating this process with varying delay times, “scans” the ion beam/pulse shape allowing a full release curve to be sampled [2].

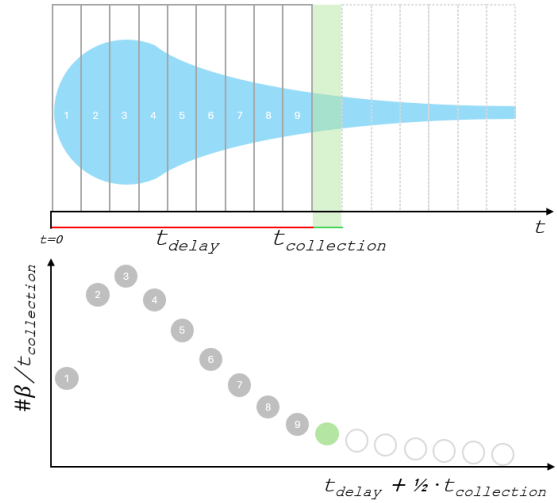


**Figure 1.** Illustration of how a release curve is collected. In the *top* panel, the blue “blob” illustrates a pulse of ions. A gray box with solid lines indicates a measured delay time, the green box is the delay time being measured and a gray box with point lines indicates a yet-to-be-measured delay time. The *bottom* panel shows the resulting release curve.

## 1.2 The Release Curve GUI Program

To facilitate the fitting of release curves at the ISOLDE control room, Simon Thomas Stegemann developed a Graphical User Interface (GUI) that allows for a straightforward fitting procedure, regardless of the user's programming expertise. This tool enables users to plot the release curve, modify the initial guess values for the fitting parameters ( $\lambda_r$ ,  $\lambda_f$ ,  $\lambda_s$ , and  $\alpha$ ), and perform chi-squared minimization. The GUI also includes options for setting refining parameters such as transmission, background counts, target temperature, and line temperature. Additionally, it allows users to select or deselect individual data points, enabling a more refined analysis of the data (Fig. 2, *left* panel). After fitting the data, the program provides a yield measurement alongside a propagated uncertainty and shows the best-fit parameters obtained from the fitting process (Fig. 2, *right* panel). When a yield is calculated, the "connect yield database" button (Fig. 2, *left* panel) enables the user to compare the estimated yield with previously recorded yields for the same atom.

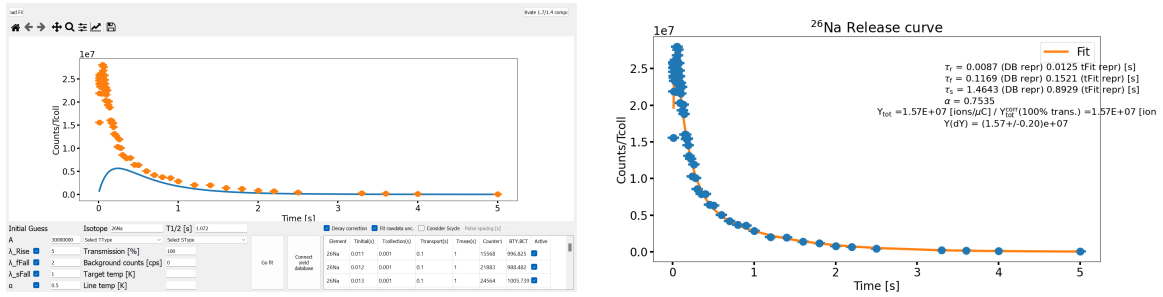


**Figure 2.** The *left* panel shows the interface of the release curve GUI, displaying the raw data points. The interface shows adjustable initial guess values for the fitting parameters ( $\lambda_r$ ,  $\lambda_f$ ,  $\lambda_s$ , and  $\alpha$ ) along with the resulting release curve, as well as optional parameters such as transmission, background counts, and temperatures. The *right* panel shows the resulting plot after fitting the release curve, displaying the optimized fit line. The plot also displays the calculated yield with propagated uncertainty  $Y(dY)$  and the best-fit values for the fitting parameters.

## 1.3 Flaws and User requests

The program in question has been in operation for several years and has undergone occasional version updates, which were provided by Simon. However, Simon is no longer available to continue development, leaving the program with some unresolved issues and unmet user requests.

- Flaws:
  1. The "connect yield database" feature is non-functional.
  2. The program crashes when a fit attempt fails.

- User requests:
  1. Ensure that all text within buttons is fully readable.
  2. Make overlaying data points distinguishable from one another.
  3. Overlay the fitted line on the data points for easier visual assessment of the fit.
  4. Prevent the displayed best-fit parameters from extending beyond the figure's boundaries.
  5. Implement numerical integration of the release curve to improve yield estimation for release curves that are challenging to fit.

My task was to address these flaws and implement the requested changes to enhance the program's functionality and usability.

## 1.4 Rebuilding the Program

The program is constructed using PyInstaller, which allows for bundling the complete Python application and all its dependencies into a single distributable executable. To create the GUI for the release curve program, it is necessary to set up an environment running Python 3.9 with the following modules: **pyqt**, **matplotlib**, **lmfit**, **pandas**, **cx-oracle**, **uarray**, **scipy**, and **pyinstaller**. It is advisable to use Miniconda or Anaconda for environment management. Additionally, to execute the **.py** files, a variable named **QT\_PLUGIN\_PATH** must be added to the environment variables, pointing to:

C:/Users/name/AppData/Local/miniconda3/Library/plugins/

The program is built using a main file called **ReleaseCurveGUI.py**, which imports several custom modules, such as **CheckBox.py**, **python\_tapefit.py**, and **PandasDisplay.py**. Ensure that the directory in which you are building the program is organized as follows:

```
my_project/
|- lib/
|   |- CheckBox.py
|   |- python_tapefit.py
|   |- PandasDisplay.py
|   |__ ...
|- ReleaseCurveGUI.py
|__ ...
```

To begin building the program, execute the following command:

```
(my_environment) c:\User\my_project> pyinstaller ReleaseCurveGUI.py
```

This command generates several files, including **ReleaseCurveGUI.spec**, which must be edited to incorporate all external modules utilized by the program. For the correct formatting of this file, refer to Appendix A.1. After making the necessary modifications, run:

```
(my_environment) c:\User\my_project> pyinstaller ReleaseCurveGUI.spec
```

Upon completion of this process, the **dist** directory will contain the distributable version of the program, including the executable that initiates the application.

## 1.5 Results

The three most significant modifications made to the program include reactivating the connection to the yield database, addressing the issue of program crashes during failed fits, and incorporating numerical integration to obtain yield measurements from raw data for cases where the release curve is non-fittable. The remaining changes were primarily aesthetic and visual enhancements (Fig. 3 *left* and *right* panel).

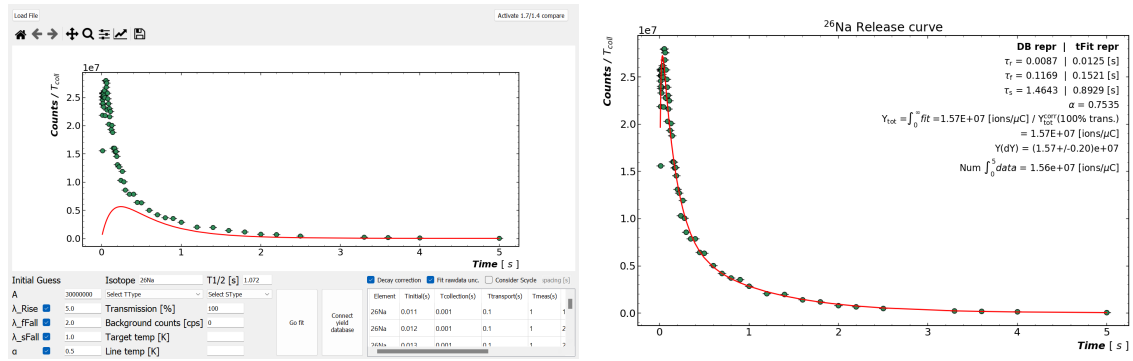


**Figure 3.** The *left* panel shows the interface of the GUI after the visual modifications. The *right* panel shows visual modifications of the fit figure as well as the addition of the numerical integration.

The reactivation of the yield database connection was achieved by updating the login password in the file **yDBcon.py**. If the password changes in the future, simply editing **yDBcon.py** in the **dist/lib/** directory to reflect the new password will restore the database connection. As seen in Fig. 4 it is now possible to compare a found yield to yields obtained from different target materials and ion sources.

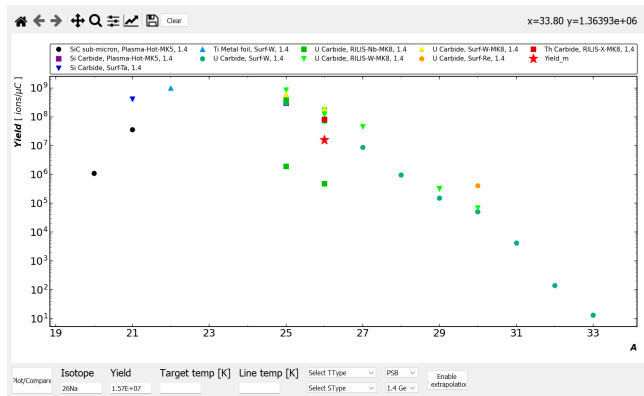


**Figure 4.** Illustration of the reconnection to the yield database plotting the yield obtained from a <sup>26</sup>Na release curve.



Although the program still occasionally fails to fit the release curves, it no longer results in a crash. The previous crashes were caused by **lmfit** returning uncertainties as type `None` when the fit was unsuccessful, leading to errors during subsequent uncertainty propagation in the script. This issue was resolved by implementing a type check in the file **python\_tapefit.py** and displaying a notification on the fit figure when the fit fails. This modification allows the user to obtain a yield measurement (albeit potentially inaccurate) even if the fit is unsuccessful.

When the three-exponential model given by Eq. (3) is found to poorly fit the data for unknown reasons, a more direct and universally applicable approach for yield determination is numerical integration. Consequently, numerical trapezoidal integration is now performed and displayed alongside the fitted data (Fig. 3 *right* panel), improving the process of yield estimation for difficult cases. The calculations are done as follows:

$$Y_i = \frac{N_{0i}}{N_p \cdot q} \cdot \varepsilon_f \int_0^\infty p(t) \cdot e^{-\lambda_i t} dt \approx \frac{1}{N_p \cdot q} \sum_{k=1}^N \frac{f_i(k-1) + f_i(k)}{2} \Delta t_k, \quad (4)$$

where  $\Delta t_k = t_k - t_{k-1}$  and  $f(k)$  represents the number of  $\beta$  – counts ( $N_{counts\ k}$ ) divided by the collection time  $t_{collection\ k}$ , and correction for the decay from transportation and measurement, for the  $k$ -th of  $N$  data points (see Eq. (5)).

$$f(k) = \frac{N_{counts\ k}}{t_{collection\ k} \cdot e^{-t_{transport\ k} \cdot \lambda_i} \cdot (1 - e^{-t_{measurement\ k} \cdot \lambda_i})} \quad (5)$$

The numerical integrator will consistently produce lower values compared to the integration of the fit function. This discrepancy arises because the numerical integrator only sums the data up to the last recorded time point,  $t_N$ , while the fit integration extends from zero to infinity, capturing the entire release curve. Consequently, the numerical method tends to underestimate the yield. The numerical integration should primarily be used as an estimate and does not account for overlapping pulses, a correction that the "Consider Scyde" option can address for the fit function. If a significant disparity exists between the numerical and fit-derived yields, even when the fit is successful, it is advisable to utilize the "Consider Scyde" function. As a rule of thumb, "Consider Scyde" should be employed when the spacing between pulses is less than one to two half-lives of the isotope being measured.

## 1.6 Further work

When fitting the release curves, the program assumes that the data points have Poisson-distributed errors. However, measuring a release curve is inherently challenging, and systematic errors are not accounted for. Figure 1 simplifies the process of measuring a release curve. In practice, each data point requires a separate proton pulse from the PSB. This introduces three major assumptions: that each released pulse of ions from the target has an identical shape, that the pulses do not overlap, and that the timing of the proton impact on the target is nearly perfect. Given that diffusion and effusion are stochastic processes, fluctuations in pulse shape are inevitable. This is evident in Fig. 5, where the data fluctuates significantly around the best fit, indicating that our model may be oversimplified or that the data point uncertainties are significantly underestimating. A more in-depth study of the systematic uncertainties in the data would likely improve the accuracy of yield uncertainties and facilitate easier fitting.

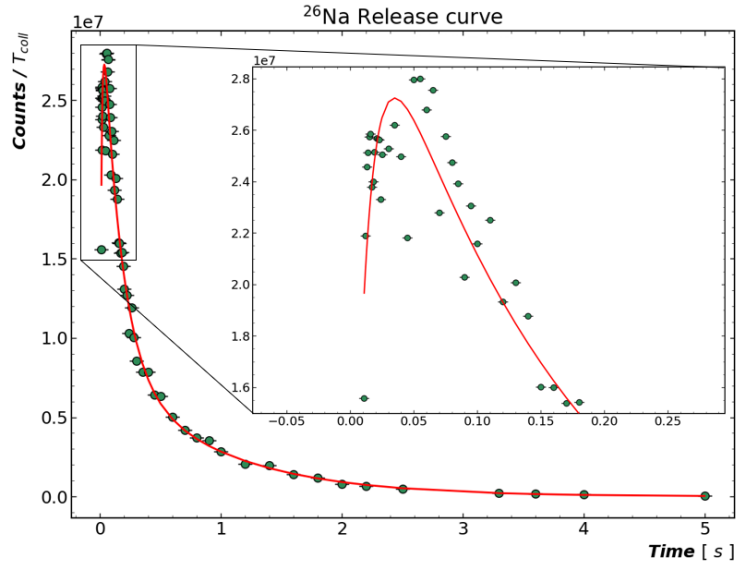
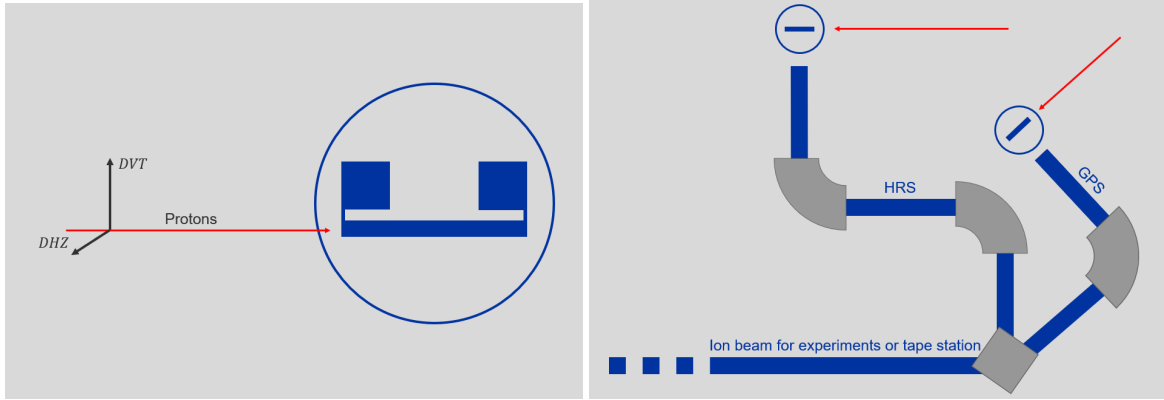


Figure 5. Zoom in on fluctuating data points.

## 2 Proton Scan

### 2.1 Background

At the ISOLDE facility, the production of radioactive ion beams from thick target materials is initiated, by irradiation of the target material using 1.4 GeV proton bunch pulses, leading to the creation of radioisotopes. To ensure that the protons strike the target material effectively, rather than any other part of the target assembly, a proton scan is performed as a standard procedure whenever a new target is being bombarded. The trajectory of the proton pulses is controlled using two dipole magnets that deflect the beam in the horizontal and vertical directions. The extent of this deflection is quantified by the current supplied to these magnets, referred to as **DVT** for dipole vertical and **DHZ** for dipole horizontal (Fig. 6 *left* panel).



**Figure 6.** The *left* panel illustrates a schematic representation of an ISOLDE target. This target consists of a long cylindrical structure made of tantalum, which encases the target material, typically uranium carbide. Two square elements within the schematic represent the heating elements used to raise the target’s temperature, thereby promoting the diffusion of the produced isotopes. Each separator at ISOLDE is fitted with its own target, as shown in the schematic view of the General Purpose and High-Resolution Separators (GPS and HRS) in the *right* panel. The beamlines from these two separators converge at a junction, from which the ions are directed either to an experimental setup or to the tape station, where the quality of the generated beam can be analyzed.

The existing procedure for performing a proton scan involves setting a specific combination of horizontal deflection current and vertical deflection current, selecting an isotope for mass separation (typically  $^{26}\text{Na}$ ), and defining both a delay time  $t_{\text{delay}}$  and a collection time  $t_{\text{collection}}$  for the tape station [3]. For each combination of current values, the extracted and separated ions are transported to the tape station, where a single point on the release curve is measured. This point is used as a measure of how much of the selected isotope is produced at the given proton trajectory.

The scanning process begins with having no horizontal deflection  $\text{DHZ} \sim 0\text{A}$ , while  $\text{DVT}$  is varied over a range of current values, typically  $[-50, 50]\text{A}$ , with a step size of  $5\text{A}$ . The  $\text{DVT}$  value that yields the highest count rate at the tape station

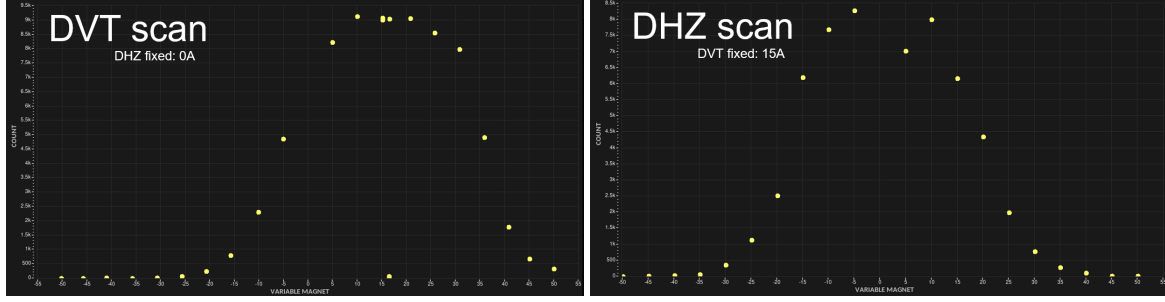


**Figure 7.** Typical proton scan produced using the tape station. The scan was done on GPS on the 30. of May 2024 between 10 : 30 and 11 : 00.

is then selected and fixed. Subsequently, DHZ is scanned over a similar range and step size. This systematic scanning identifies an approximate optimal current setting for maximizing the yield at the tape station. Fig. 7 shows a usual scan of DVT in the *left* panel and DHZ in the *right* panel.

When one of the ISOLDE separators is employed for a proton scan, the other separator cannot be used simultaneously, as the tape station is engaged, as illustrated in Fig. 6 *right* panel. To address this limitation, it was hypothesized that the radiation monitors in the target rooms could be utilized instead of the tape station. Although this approach only provides a measure of the total isotope production rather than the yield of ions, it offers a useful alternative. By using both the radiation monitors and the tape station for testing, validation of the optimal current settings found by the radiation monitors is possible, ensuring that the same maximum is identified in both cases. Furthermore, since time is less of a problem when using the radiation monitors it enables the possibility of executing two-dimensional proton scans, wherein both the vertical and horizontal deflections can be scanned across their full ranges.

## 2.2 The script

My task involved developing a script capable of collecting data from both the vertical and horizontal magnets, as well as identifying the corresponding radiation levels associated with the current settings. Upon acquiring the data, the script generates visualizations of one-dimensional and two-dimensional proton scans.

### 2.2.1 Data

The current setting of DVT and DHZ and the radiation monitors are uploaded to NXCALS [4] and can be accessed through a Spark Cluster. Instructions for connecting to the Spark Cluster using SWAN are provided in Appendix A.2, Fig. 23. The data acquisition for these devices is synchronized with the proton pulses from the PSB. Since the PSB delivers pulses every 1.2s [1], this interval determines the timing for data collection from the measuring devices. To minimize the amount of data on

the database DHZ and DVT are set to publish values only when there is a change in the set currents. It is important to note that not all PSB pulses are directed to ISOLDE, rendering much of the acquired data irrelevant for proton scan analysis. A variable from NXCALS called the PSB telegram is used to identify the data points of interest. The telegram contains information about which users receive protons and at which times. In summary, the variables used for GPS and HRS can be found in Tab. 2. These variables are loaded into a Python script using the Pytimber library.

	DVT ( <i>BTY.</i> )	DHZ ( <i>BTY.</i> )	Monitors	Telegram ( <i>PSB.</i> )
<b>GPS</b>	DVT212:I_MEAS	DHZ211:I_MEAS	PMHIS201:RAW	TGM:USER
<b>HRS</b>	DVT324:I_MEAS	DHZ323:I_MEAS	PMHIS202:RAW	

**Table 1.** Table of variable names. The italicized three-letter abbreviations represent the variable hierarchy, which functions like a directory where the variable is stored. When referencing a variable, its hierarchy should precede the variable name.

### 2.2.2 Analysis

For each proton pulse from the PSB delivered to either the GPS or HRS, there is a corresponding data point for the proton scan. The telegram provides the times of interest (TOI) necessary for this analysis. Both deflecting dipole magnets are synchronized with the telegram timing; however, due to the limited publishing frequency of the current data, if a current value cannot be located for the exact TOI, the script defaults to the most recent recorded current value prior to the TOI. The radiation monitors, in contrast, are not perfectly synchronized with the telegram and generally exhibit a delay. To address this issue, the script selects the highest radiation monitor value recorded between the moment when proton pulse  $i$  occurs and the subsequent proton pulse  $i + 1$ . To ensure that the selected value corresponds to the prompt radiation from a proton pulse, a minimum radiation threshold of 0.5 Gy/h for HRS and 1 Gy/h for GPS is imposed, see Fig. 8. If this criterion is not met, the data point is discarded. This cut-off is based on the assumption that some of the telegram pulses may be empty.

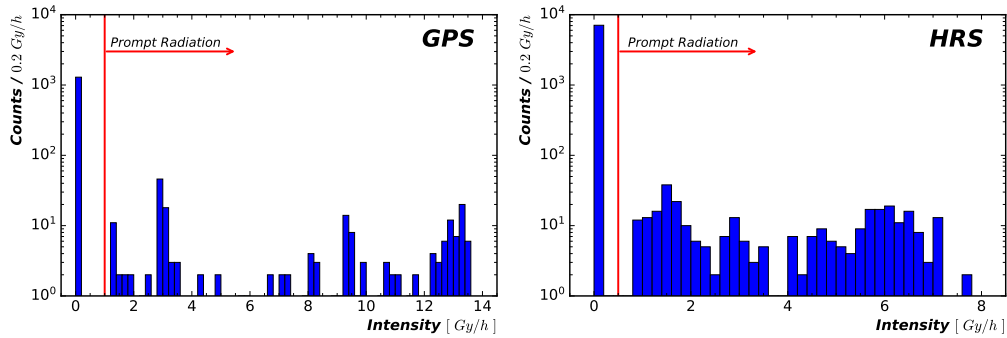


**Figure 8.** Proton scan dose levels data from both GPS (*left panel*) and HRS (*right panel*) display the threshold values established for detecting prompt radiation.

The straightforward nature of the data handling allows the user to import and filter the data by simply specifying the start and end times of the scan ( $t_{start}$  and  $t_{end}$ ), the separator used (GPS or HRS), and the type of scan performed (1D or 2D). While specifying the step size of the scan is also recommended, it is not required. If the step size is not provided, the program automatically determines the most common change in current and assumes this as the step size.

## 2.3 Results

By collecting the data from the radiation monitors from the proton scan done in Fig. 7 the results of the two methods can be compared. Figure 9 shows the time series data after filtering for the proton pulses delivered to GPS and for prompt radiation, whereas Fig. 10 shows the resulting proton scan.

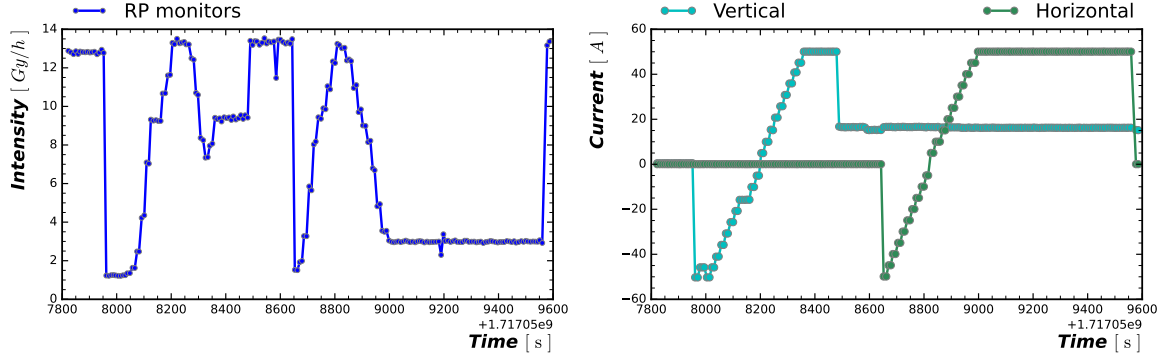


**Figure 9.** Time series data filtered for proton pulses delivered to GPS and for instances of prompt radiation. Radiation Protection (RP) monitors are the radiation monitors, Vertical is DVT, and Horizontal is DHZ.

From Fig. 10, it is apparent that the radiation monitors capture the overall shape of the data observed at the tape station, though they also detect additional contributions around the distribution tails. The counts recorded by the tape station are influenced by several factors, including the number of produced radioisotopes, their release efficiency, ionization efficiency, and transport efficiency, as discussed in Sec. 1.1. In contrast, the dose measured by the radiation monitors in the target room is primarily dependent on the number of produced radioisotopes. Consequently, the distribution captured by the tape station can be considered a subset of the distribution observed by the radiation monitors. This suggests that the radioisotopes produced within the tails of the radiation monitor distribution are those that were not successfully released from the target.

The likelihood of proton-nucleus collisions is primarily determined by the nuclear cross-section  $\sigma$ , the material density  $\rho$ , and the distance  $d$  traversed by the proton bunch through the material [5]. Given that,  $d$  is mostly constant for protons interacting with the target, changes in the probability of proton-nucleus collision

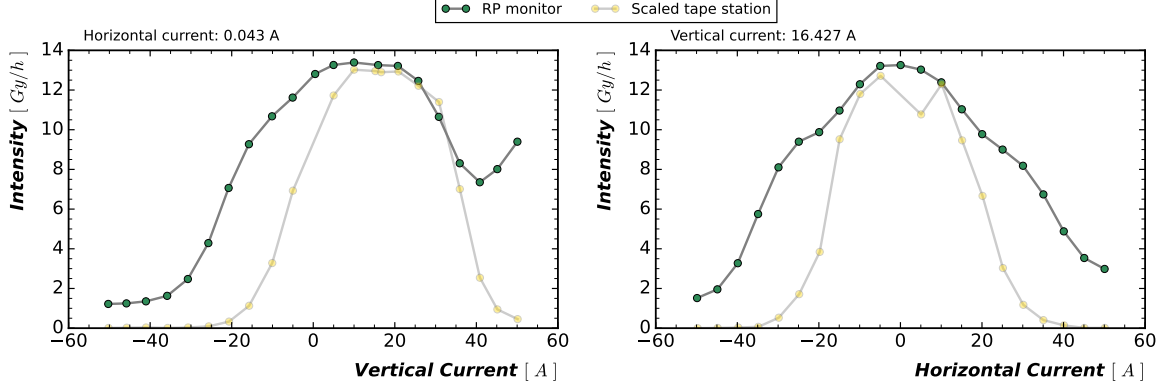


**Figure 10.** Radiation monitor measurements from proton scan. Alongside the measured radiation levels is a scaled version of the data from Fig 7 for visual comparison between the two methods. The target material used was UC<sub>x</sub> palets

predominantly reflect variations in  $\rho$  or  $\sigma$ . In other words, a larger target ( $\sigma$ ) and more densely packed target ( $\rho$ ), result in a greater likelihood of a successful collision. However, the production of radioactive species is closely tied to spallation, fragmentation, and fission reactions, which are also highly material-specific processes. Therefore the measured radiation levels are a measure of changes in target density and composition, effectively providing an almost x-ray-like image of the target that reveals valuable insights about the target geometry. The additional tails in the radiation monitor distribution may for instance be attributed to protons striking the tantalum container surrounding the uranium carbide target material. This would explain why the produced radioisotopes in the tails of the radiation monitor distribution have little contribution to the  $^{26}\text{Na}$  counts measured at the tape station.

Switching the target material from uranium carbide pellets to tantalum carbide powder modifies both the nuclear cross-section  $\sigma$  and the material density  $\rho$ , resulting in significant changes in the measurements. Figure 11 illustrates a coarse two-dimensional proton scan (with a step size of 7A for both DVT and DHZ) of the tantalum carbide target, heated with a current of 601.85A. In the *left* panel, data from the tape station suggest that hitting the center of the material no longer is the most effective strategy. This inefficiency arises because the radioisotopes generated in the middle of the target have a reduced mean free path due to the increased material density, leading to longer diffusion times to the ion source. In contrast, directing the proton beam closer to the ion source at the top of the target increases the mean free path, thus improving isotope release. The *right* panel, which displays results from the radiation monitors, indicates that the new target material produces less radioactivity than compared to the tantalum casing. Additionally, it reveals that the density of the tantalum carbide within the target varies, likely due to gravity.

Further heating the target to 682.8A and reducing the scan step size to 4A for both DVT and DHZ resulted in the observations shown in Fig. 12. The *left* panel indicates that increasing the target temperature enables faster diffusion of isotopes

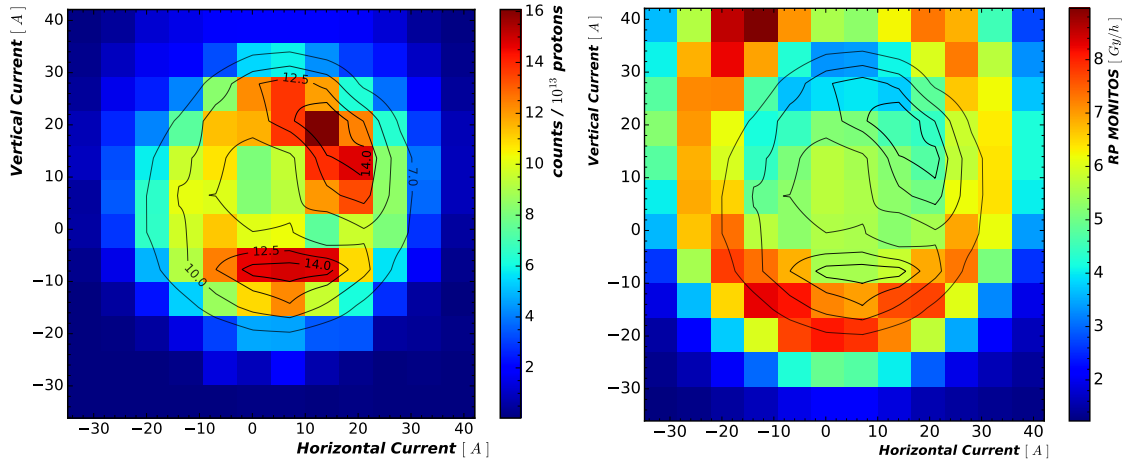


**Figure 11.** The *left* panel shows a 2D protonscan produced using the tape station. Contour line of 7, 10, 12.5, and 14 counts per  $10^{13}$  protons has been added. The *right* panel shows the same 2D proton scan using the radiation monitors. The contour lines from the tape station distribution have been overlayed for easy comparison. The current supplied to the target for heating was 601.85A. Step size for scan was 7A for both DVT and DHZ.

produced in the center to the ion source. However, the "donut-like" pattern around the target material persists, implying that it remains advantageous to target the less dense upper region of the material, where the increased mean free path for the produced radioisotopes enhances their release. The *right* panel shows that the elevated temperature does not significantly impact the radiation levels, suggesting that the number of produced ions remains relatively constant. Consequently, the increase in counts per protons observed in the *left* panel is likely attributable solely to the faster diffusion process.

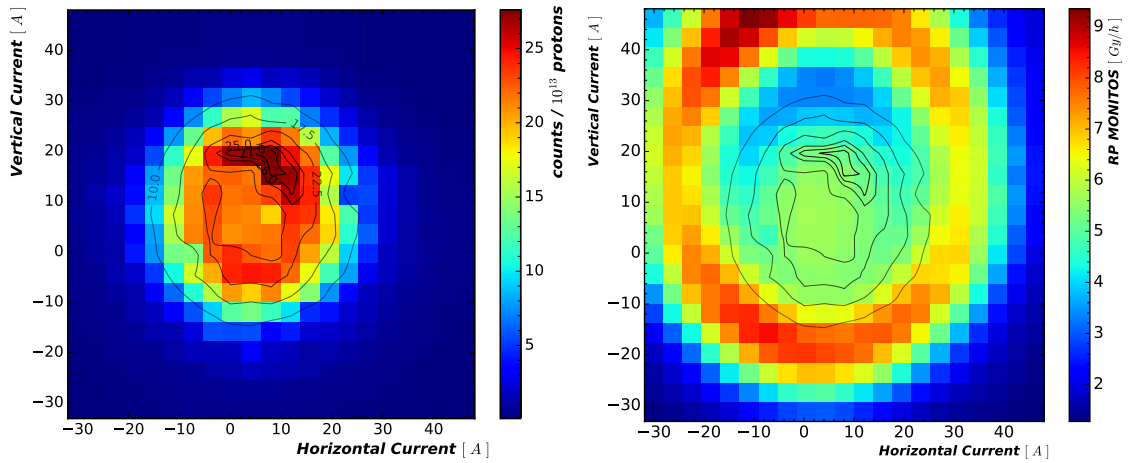


**Figure 12.** The *left* panel shows a 2D protonscan produced using the tape station. Contour line of 10, 17.5, 22.5, 25, 26, and 27 counts per  $10^{13}$  protons has been added. The *right* panel shows the same 2D proton scan using the radiation monitors. The contour lines from the tape station distribution have been overlayed for easy comparison. The current supplied to the target for heating was 682.8A. Step size for scan was 4A for both DVT and DHZ.



## **2.4 Further work**

As of the writing of this report, the radiation monitors experience an upload delay of approximately two hours. This significant delay currently prevents the radiation monitors from being used as a real-time tool for conducting proton scans, as the delay is too substantial to provide timely feedback. To enable the use of these monitors as a live scanning instrument in the future, it is essential to address and reduce this upload delay. Resolving this issue would pave the way for the development of a more permanent, standalone program for performing radiation monitor proton scans, eliminating the need for reliance on the SWAN platform.

### 3 Study of $^{229}\text{Ra}$

#### 3.1 Background

Ultraprecise timekeeping primarily depends on atomic clocks, which operate by using lasers tuned to specific frequencies to excite electron states. These electrons transition to higher energy levels and then return to lower states at rapid, consistent intervals, generating the "tick" of an atomic clock. However, atomic clocks are not without limitations, as the electron states are sensitive to external perturbations from magnetic and electric fields, compromising their accuracy. To enhance precision in timekeeping technologies, researchers are exploring the possibility of shifting timekeeping to the

atomic nucleus, which is better protected from external disturbances. This approach involves exciting the energy states of protons and neutrons rather than electron states, creating what is known as a nuclear isomer. Typically, the excitation energies of isomeric nuclear levels range from a few tens of keV to several MeV, making them unattainable to excite with current laser technologies [6]. However, measurements of the transition energy from thorium-229 ( $^{229}\text{Th}$ ) to its isomeric state ( $^{229\text{m}}\text{Th}$ ) have revealed an exceptionally low excitation energy of only 8.338(24)eV [7]. This low energy makes excitation feasible using vacuum-ultraviolet photons and brings the possibility of developing a nuclear clock closer to reality.

An ISOLDE target comprised of uranium carbide can be heated to temperatures  $\sim 2000^\circ\text{C}$ . However, operating at higher temperatures significantly reduces the target's lifespan, rendering these temperatures unsustainable for long-term production. This limitation, combined with the extremely high melting and boiling points and low vapor pressures of certain elements, renders some elements highly non-volatile and thus unavailable as ion beams at ISOLDE [8]. Unfortunately, thorium is one such element that cannot be directly produced as a beam at ISOLDE. Consequently, an alter-

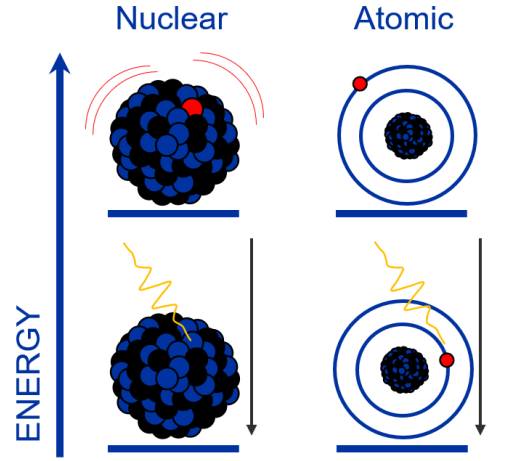


**Figure 13.** Illustration of the state transitions of a nucleus and an electron.

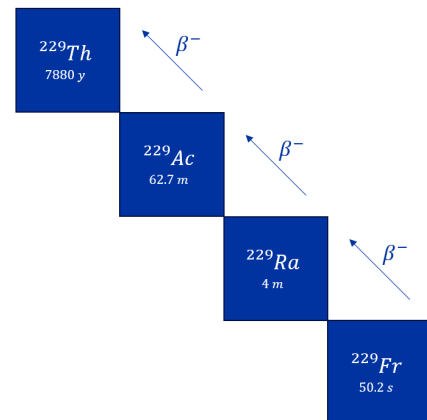


**Figure 14.** Illustration of the  $\beta$ -decay chains feeding the production of  $^{229}\text{Th}$

native method for generating  $^{229}\text{Th}$  is required. By producing an  $^{229}\text{Fr}$ ,  $^{229}\text{Ra}$ , and  $^{229}\text{Ac}$  ion beams a link of  $\beta$ -decay chains are produced all ending at the metastable  $^{229}\text{Th}$  as shown in Fig. 14. These isotopes are then implanted into a large-bandgap crystal. To determine the number of implanted  $^{229}\text{Fr}$ ,  $^{229}\text{Ra}$ , and  $^{229}\text{Ac}$ , ultimately revealing the number implanted  $^{229}\text{Th}$  a precise gamma spectrum analysis is needed. However, limited studies have been done on  $^{229}\text{Ra}$ , and the isotope has no recorded gamma lines or branching ratios. In the release of the nature article measuring the transition energy of  $^{229m}\text{Th}$  four new gamma lines (355 keV, 445 keV, 463 keV, and 502 keV) were reported as potential  $^{229}\text{Ra}$  lines, but no branching ratios were uncovered [7].

My task was to utilize existing datasets from the tape station for  $^{229}\text{Fr}$ ,  $^{229}\text{Ra}$ , and  $^{229}\text{Ac}$  ion beams to identify new gamma lines and determine their associated branching ratios for  $^{229}\text{Ra}$ .

### 3.2 Calibration

Before conducting any analysis, it is essential to verify that the measuring device is properly calibrated. For the germanium (Ge) gamma detector, two types of calibrations were performed: **energy** calibration and **efficiency** calibration.

An *energy calibration* is performed using a well-established calibration source, typically  $^{152}\text{Eu}$ , which emits gamma rays across a broad spectrum of energies, typically ranging from 120 keV to 1400 keV. To determine the energy corresponding to each detector channel, the centroid of each gamma peak is identified through a Gaussian fit, with the background modeled using either a linear or polynomial function. The relationship between the detector's channel numbers and the actual gamma-ray energies is then derived by fitting the centroid channel values to the known energies of the  $^{152}\text{Eu}$  peaks using a second-degree polynomial function. The calibration curve and corresponding results are presented in Fig. 15.

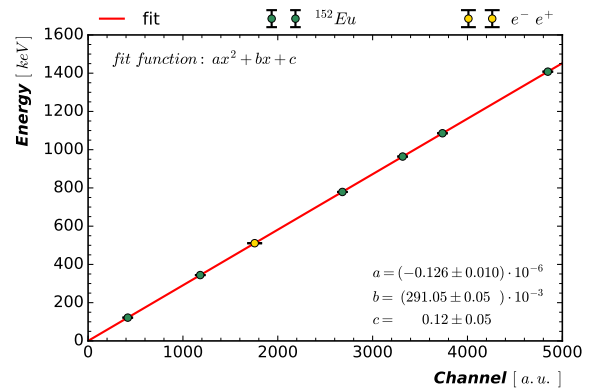


**Figure 15.** Energy calibration of the tape station Ge detector using  $^{152}\text{Eu}$  and the peak of electrons-positrons annihilation.

An *efficiency calibration* is similarly conducted using a well-characterized calibration source. The peaks are once again fitted using a Gaussian function with an appropriate background model; however, this calibration focuses on the mea-

sured counts in each peak and not the peaks' position. To achieve this, a source with well-documented branching ratios and known initial activity is required, as the calibration involves calculating the efficiency  $\epsilon_i = N_{\text{measured } i} / N_{\text{emitted } i}$ , where  $i$  denotes the peak index,  $N_{\text{measured } i}$  represents the number of counts obtained from the fit, and  $N_{\text{emitted } i}$  is the actual number of emitted photons. Such a calibration was performed on March 3, 2022, by removing the Ge detector from the tape station and placing a  $^{152}\text{Eu}$  source at the same distance from the detector as the irradiated tape would be during measurements. Since the measured count rates are highly sensitive to the detector's geometry and the position of the implanted source on the tape, an in-situ (online) calibration was conducted. In theory, the results of both calibrations should be closely aligned, with only minor differences; however, the online calibration is expected to more accurately reflect the actual geometry of the detector setup.

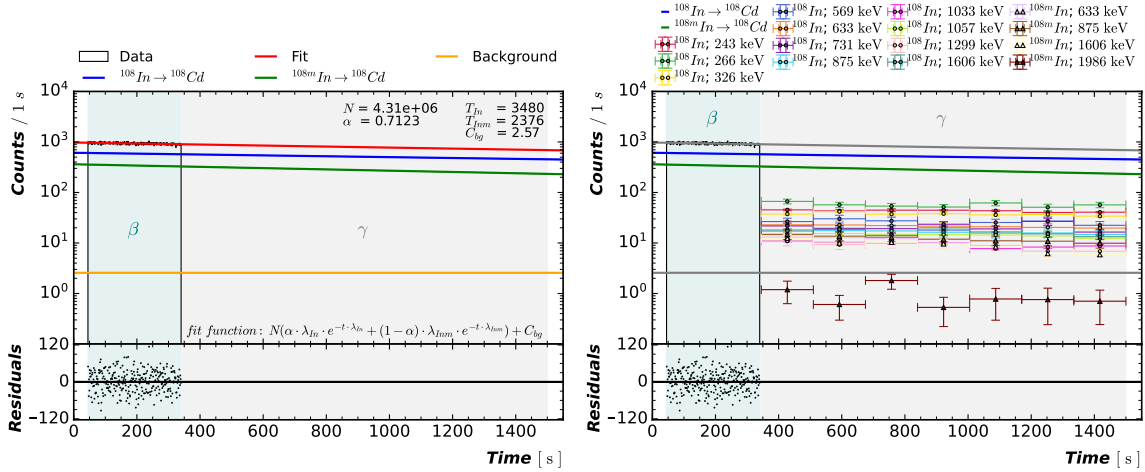


**Figure 16.** The *left* panel shows the fit of the beta decay rates. For this fit  $\alpha$ ,  $T_{In}$ ,  $T_{Inm}$ , and  $C_{bg}$  was fixed, only fitting for  $N$ . The *right* panel shows the rates obtained from the gamma peaks in time intervals of 165s.

An online analysis was conducted using a dataset that measured the beta decays and gamma emissions of  $^{108}\text{In}$  and its isomer  $^{108m}\text{In}$ . To determine the fraction of  $^{108m}\text{In}$  produced relative to the combined total production of both the ground state and the isomer, the gamma peaks were analyzed. This analysis applied the calibration from 2022, comparing the 1986.3 keV peak of  $^{108m}\text{In}$  with non-overlapping peaks of  $^{108}\text{In}$  (see Appendix A.3, Fig. 24). The resulting ratio was calculated as  $1 - \alpha_\gamma = \frac{N_{108m\text{In}}}{N_{108\text{In}} + N_{108m\text{In}}} = 0.2709$ . However, this ratio reflects the conditions at the time of the gamma measurement, and since the half-lives of  $^{108}\text{In}$  (58 minutes) and  $^{108m}\text{In}$  (39.6 minutes) differ, the ratio is not constant in time. The wanted fraction is the fraction at the start of the beta-decay measurement. The interval between the midpoint of the gamma measurement and the start of the  $\beta$  measurement is approximately  $-900$  s. Applying Eq. (7) at this time adjusts the ratio, providing the value at the beginning of the beta-decay measurement.

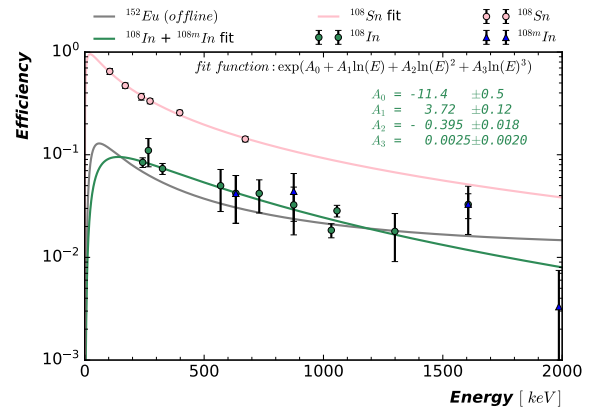
$$(1 - \alpha(t)) = \frac{N_{108m\text{In}}(t)}{N_{108m\text{In}}(t) + N_{108\text{In}}(t)} = \frac{(1 - \alpha_\gamma)e^{-\lambda_{108m\text{In}} \cdot t}}{(1 - \alpha_\gamma)e^{-\lambda_{108m\text{In}} \cdot t} + \alpha_\gamma e^{-\lambda_{108\text{In}} \cdot t}} \quad (6)$$

$$(1 - \alpha(-900\text{s})) = (1 - \alpha_0) = 0.2877$$

The derived fraction facilitates the fitting of the beta-decay rates, enabling the fitting of the temporal evolution the activities of the ground state and isomere ( $A_{108\text{In}}$  and  $A_{108m\text{In}}$ ), as depicted in the *left* panel of Fig. 16. For the gamma emissions, all relevant peaks corresponding to both the ground state and the isomer were fitted across varying time intervals, with the resulting counts corrected according to their respective branching ratios. Overlapping peaks from the ground state and isomer were separated using the formulas provided in App. A.4. By comparing the gamma rates with the calculated activities, an efficiency measurement for each peak was obtained for each time interval,

$$\epsilon_i(t_j + \Delta/2) = \frac{N_{\text{measured } ij}}{B_i \Delta t} / A_{\text{emitted } i}(t_j + \Delta t/2). \quad (7)$$

Here,  $[t_j, t_j + \Delta t]$  represents the  $j$ -th time interval of width  $\Delta t$ , during which gamma emissions are fitted,  $B_i$  denotes the branching ratio of peak  $i$ , and  $N_{\text{measured } ij}$  is the count's obtained from fitting peak  $i$  for the  $j$ -th time interval. The term  $\frac{N_{\text{measured } ij}}{B_i \Delta t}$  is shown as the data points in the *right* panel of Fig. 16. This quantity is divided by  $A_{\text{emitted } i}(t_j + \Delta t/2)$ , which is derived from the beta decay fit, represented by the blue and green lines for  $A_{108\text{In}}$  and  $A_{108m\text{In}}$ , respectively. A single efficiency value per peak is determined by averaging the efficiency over time, which is then used for efficiency calibration, as depicted in Fig. 17.



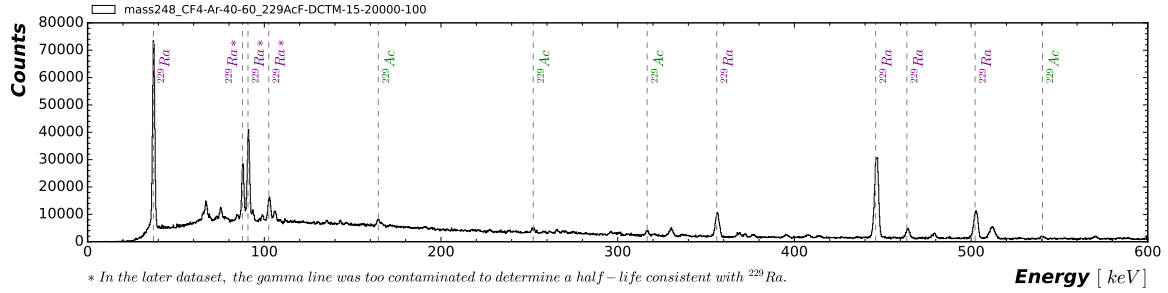
**Figure 17.** Efficiency calibration of the tape station Ge detector using  $^{108}\text{In}$  and  $^{108m}\text{In}$ . For comparisons the offline  $^{152}\text{Eu}$  calibration is also plotted as well as a failed online  $^{108}\text{Sn}$  calibration.

Figure 17 compares the online calibration of indium with the offline calibration using europium. The figure shows that no efficiency measurements were obtained in the X-ray energy range, rendering the calibration in this region unreliable. Additionally, a calibration using tin ( $^{108}\text{Sn}$ ) is included, but it was discarded due to inaccuracies in the beta decay measurements. This fit is supplied solely to illustrate the challenges associated with online calibrations and is not considered valid.

### 3.3 Analysis and results

#### 3.3.1 Radioactive molecular beam dataset

The technique of extracting radioisotopes as molecular beams is employed for the mass separation of isobaric elements. By introducing  $^{19}\text{F}$  gas into the target, various molecules are formed based on the chemical properties of the elements. Specifically, in this case,  $^{229}\text{Fr}$ ,  $^{248}\text{RaF}$ , and  $^{267}\text{AcF}_2$  are produced, enabling the separation of these isotopes. Selecting the mass number 248 for the mass separator results in a nearly pure gamma spectrum for  $^{229}\text{Ra}$ . However, the absence of beta-decay measurements in this dataset prevents the determination of the yield for  $^{229}\text{Ra}$  and prevents the calculation of branching ratios. Despite this, the dataset is useful for identifying gamma peaks with half-lives consistent with that of  $^{229}\text{Ra}$ , which is 240 s. These identified peaks are illustrated in Fig. 18.



**Figure 18.** Gamma spectrum from radioactive molecular beam dataset with the separator set to mass number 248. Identified gamma lines with consistent half-lives to that of  $^{229}\text{Ra}$  are marked with a dashed line and a purple label. Identified  $^{229}\text{Ac}$  gamma lines are indicated with a dashed line and a green label. The spectrum is calibrated for both energy and efficiency.

By fitting the suspected peaks with a Gaussian function and a linear background, the centroid and count for each peak are determined. Although an absolute branching ratio cannot be obtained, a relative branching ratio can be calculated, as illustrated in Fig. 19. Due to substantial contamination of the three X-ray gamma lines marked with a \* in Fig. 18 in other datasets, deriving relative branching ratios provides a useful approximation for later analysis to estimate the absolute branching ratios of these gamma lines.

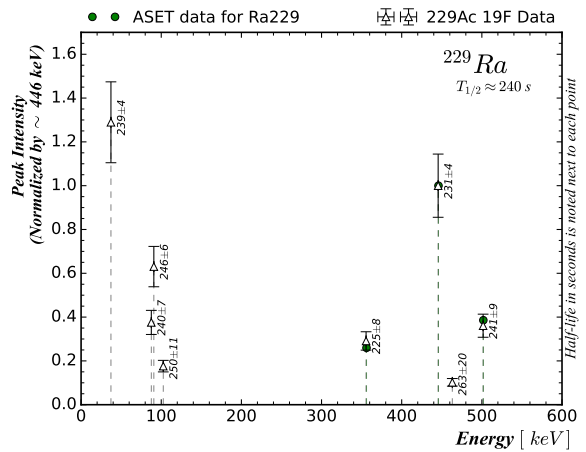


**Figure 19.** Branching ratio (peak intensity) relative to the area the 446keV gamma line. The found half-life and fit uncertainty are noted next to each data point. The green data points are the normalized intensities found by Silvia Bara and her team for comparison.

### 3.3.2 Ion beam dataset

In this dataset, the isotopes  $^{229}\text{Fr}$ ,  $^{229}\text{Ra}$ , and  $^{229}\text{Ac}$  are all present and it includes both beta decay and gamma emission measurements. However, due to significant contamination of the gamma lines of 87.6 keV, 90.8 keV, and 102.5 keV, they were excluded from the analysis. Given that the three isotopes decay into one another (as illustrated in Fig. 14), the Bateman equation was employed to model the temporal evolution of activities when fitting the beta decay rates. The resulting fit, along with the Bateman equation used, is depicted in Fig. 20, *left* panel.

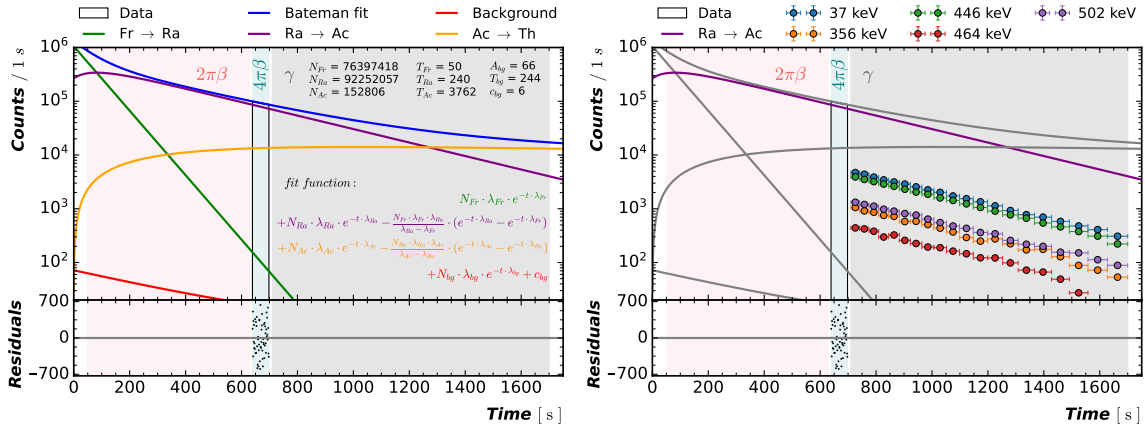


**Figure 20.** The *left* panel shows the fit of the beta decay rates using the Bateman equation. For this fit  $T_{Fr}$ ,  $T_{Ra}$ ,  $T_{Ac}$ ,  $A_{bg}$ ,  $T_{bg}$ , and  $C_{bg}$  was fixed, only fitting for  $N_{Fr}$ ,  $N_{Ra}$ , and  $N_{Ac}$ .  $A_{bg}$ ,  $T_{bg}$ , and  $C_{bg}$  were determined from fitting the background in a separate fit. The *right* panel shows the rates obtained from fitting the identified  $^{229}\text{Ra}$  gamma peaks in logarithmic time intervals. The colored time regions in the figures are shown when different measurements were taken. The  $2\pi\beta$  is a beta detector with a solid angle coverage of  $2\pi$ ,  $4\pi\beta$  has a solid angle coverage of  $4\pi$ , and  $\gamma$  is the Ge gamma detector.

The method used for determining the branching ratios is analogous to the process used to derive the efficiency calibration for the Ge detector discussed in Sec. 3.2, with the key difference being that, in this case, the efficiency is already known, but the branching ratio is not. By fitting the gamma lines at 37.5 keV, 356.0 keV, 446.1 keV, 463.7 keV, and 502.1 keV over different time intervals, the peak activity as a function of time can be measured as shown in Fig. 20 *right* panel. The ratio between the measured peak activities and the fitted  $^{229}\text{Ra}$  beta activity (representing the total activity) yields the branching ratio. Since each peak is fitted multiple times across different time intervals, a temporal branching ratio is obtained as shown in Fig. 21. As the data in the gamma peaks became sparse over time, logarithmic time intervals were selected to main-

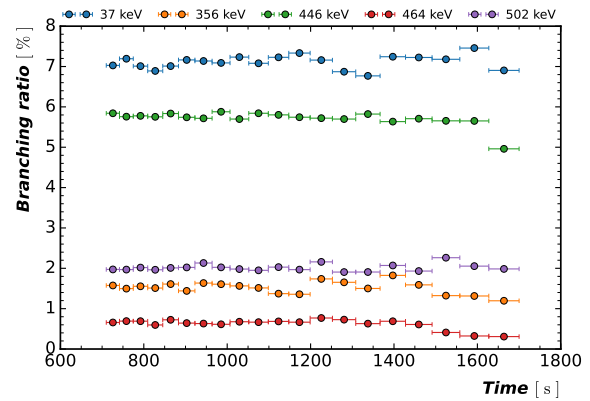


**Figure 21.** Temporal branching ratios for five of the identified  $^{229}\text{Ra}$  gamma lines.



tain data consistency. Despite this adjustment, increasing fluctuations in data points are still observed at later times. To derive a final value for the branching ratios, the data were truncated at times exceeding 1400 s, and the resulting peak values were plotted as histograms, as shown in Fig. 22. The histograms include one-sigma confidence intervals, indicated by colored shaded regions, and the median branching ratio for each distribution is represented by a solid line of the same color. The branching ratios for the three gamma lines previously determined as contaminated in this dataset were obtained using the relative branching ratios shown in Fig. 19 and the median value for the 446.1 keV gamma line. These are indicated by black vertical lines with different line styles along with gray-shaded regions indicating the one-sigma confidence intervals.

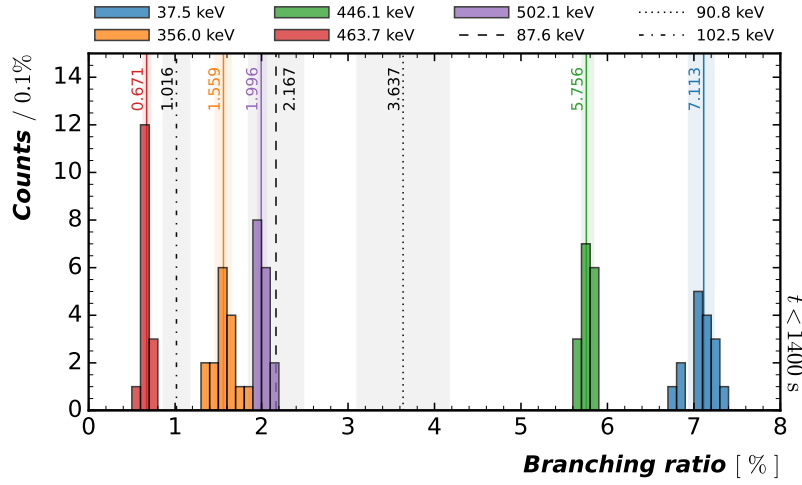


**Figure 22.** Histograms of the branching ratios for the five analyzed gamma lines of  $^{229}\text{Ra}$  are presented, with the shaded areas representing the one-sigma confidence intervals, and the vertical lines denoting the median values. The branching ratios, indicated by black vertical lines, were determined by combining the relative branching ratios shown in Fig. 19 with the median value of the 446.1 keV line.

$E_\gamma$ [keV]	$I_\gamma$ [%]
37.5	$7.11^{+0.12}_{-0.18}$
87.6	$2.2 \pm 0.3$
90.8	$3.6 \pm 0.5$
102.5	$1.02 \pm 0.15$
356.0	$1.56^{+0.09}_{-0.10}$
446.1	$5.76^{+0.08}_{-0.05}$
463.7	$0.67^{+0.04}_{-0.04}$
502.1	$2.00^{+0.06}_{-0.04}$

**Table 2.** Summary table of the results from the analysis



### 3.4 Further work

The primary source of uncertainty in this analysis is suspected to stem from the efficiency calibration, and this uncertainty is not been propagated into the branching ratio confidence intervals. The lack of data points in the X-ray region of the efficiency calibration makes the branching ratios in the 0 to 100 keV range somewhat unreliable. For future studies, it would be beneficial to perform a more precise on-line efficiency calibration and to conduct a more thorough analysis of the associated uncertainties.

Furthermore, the efficiency of the  $2\pi$   $\beta$  detector remains undetermined, which prevents the integration of its data into the Bateman fits. To enhance the robustness of the analysis, it is recommended that the efficiency of the  $2\pi$   $\beta$  detector be determined. Alternatively, this detector's data could be utilized to estimate the initial ratios between  $^{229}\text{Fr}$ ,  $^{229}\text{Ra}$ , and  $^{229}\text{Ac}$ . Another viable approach would be to acquire a new dataset using only the  $4\pi$   $\beta$  detector, extending the measurement duration to improve the accuracy of yield determinations and the precision of the calculated branching ratios.

# A Appendix

## A.1 Formating of ReleaseCurveGUI.spec

```
# -*- mode: python ; coding: utf-8 -*-

block_cipher = None

a = Analysis(
    ['ReleaseCurveGUI.py'],
    pathex=[],
    binaries=[],
    datas=[
        ('lib/CheckBox.py', 'lib'),
        ('lib/isotopes.txt', 'lib'),
        ('lib/PandasDisplay.py', 'lib'),
        ('lib/python_tapefit.py', 'lib'),
        ('lib/RcurveEcompLIB.py', 'lib'),
        ('lib/yDBcon.py', 'lib'),
        ('lib/yieldExtrapolation.py', 'lib')
    ],
    hiddenimports=[
        'scipy.special._cdfplib',
        'pandas',
        'lmfit',
        'cx_Oracle',
        'mplcursors',
        'screeninfo',
        'uncertainties',
        'uncertainties.unumpy',
        'scipy'
    ],
    hookspath=[],
    runtime_hooks=[],
    excludes=[],
    win_no_prefer_redirects=False,
    win_private_assemblies=False,
    cipher=block_cipher,
)

pyz = PYZ(a.pure, a.zipped_data, cipher=block_cipher)

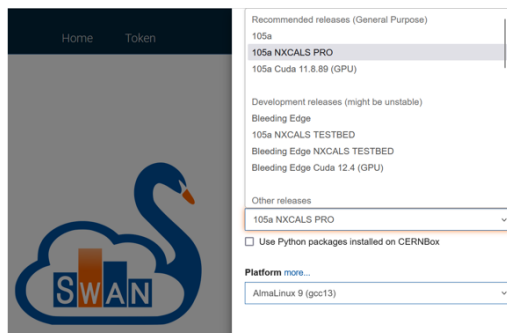
exe = EXE(
    pyz,
    a.scripts,
```

```
[],
exclude_binaries=True,
name='ReleaseCurveGUI',
debug=False,
bootloader_ignore_signals=False,
strip=False,
upx=True,
console=True,
disable_windowed_traceback=False,
argv_emulation=False,
target_arch=None,
codesign_identity=None,
entitlements_file=None,
)

coll = COLLECT(
    exe,
    a.binaries,
    a.zipfiles,
    a.datas,
    strip=False,
    upx=True,
    upx_exclude=[],
    name='ReleaseCurveGUI',
)
```

## A.2 Connecting to the spark cluster

Pick 105a *NXCALS PRO* as your Software stack.



Click the star icon, log in, and check the box “include NXCALS options”. Click connect.

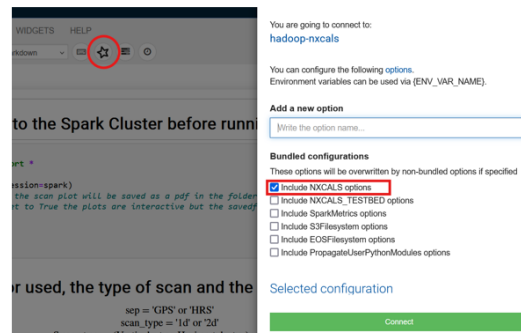


**Figure 23.** How to connect to the Spark Cluster using swan. For a more in-depth description visit: <https://confluence.cern.ch/display/RBS/Accessing+data+from+TIMBER+using+SWAN>

### A.3 Finding ratios of $^{108m}\text{In}$ to $^{108}\text{In}$

In108					In108m			
Energy (keV)	Area	Area/efficiency	Branching	Ratio	Energy (keV)	Area	Area/efficiency	Branching
876.7	2.09E+04	8.83E+05	100	0.2470	1986.8	5.30E+02	3.59E+04	12.4
1034.2	4.01E+03	1.91E+05	35	0.3469				
1058	5.31E+03	2.57E+05	29	0.2465				
1301.2	2.46E+03	1.36E+05	15.1	0.2435				
325.6	5.75E+03	1.07E+05	13.7	0.2704				
				0.2709				

**Figure 24.** screenshot of the table used to find the ratio between  $^{108m}\text{In}$  to  $^{108}\text{In}$  produced in the ion beam.

### A.4 splitting overlapping gamma peaks

The fraction of groundstate in time can be found using Eq. 7 denoted as  $\alpha$ . Fitting the two overlapping peaks the summed number of gammas is obtained

$$N = N_G + N_I. \quad (8)$$

However, the overlapping peaks will have different branching ratios so correcting for these ratios gives

$$\tilde{N} = \frac{N_G}{B_G} + \frac{N_I}{B_I}. \quad (9)$$

Since the branching ratios were considered when calculating  $\alpha$  the following must be true,

$$\frac{N_G}{B_G} = \alpha \tilde{N} \quad (10)$$

$$\frac{N_I}{B_I} = (1 - \alpha) \tilde{N} \quad (11)$$

By combining these four equations, two equations for finding  $\frac{N_G}{B_G}$  and  $\frac{N_I}{B_I}$  is found:

$$\frac{N_G}{B_G} = \frac{N\alpha}{\alpha B_G + B_I(1 - \alpha)} \quad (12)$$

$$\frac{N_I}{B_I} = N \left( 1 - \frac{\alpha B_G}{\alpha B_G + B_I(1 - \alpha)} \right) \quad (13)$$

## References

- [1] Simon Albright et al. New longitudinal beam production methods in the CERN proton synchrotron booster. IPAC2021:4.
- [2] J Ballof et al. The upgraded isolde yield database—a new tool to predict beam intensities. *Nuclear Instruments and Methods in Physics Research Section B: Beam Interactions with Materials and Atoms*, 463:211–215, 2020.
- [3] S Stegemann, D Atanasov, M Au, et al. The cern-isolde fast tape station. *Nuclear Instruments and Methods in Physics Research Section B: Beam Interactions with Materials and Atoms*, 541:169–172, 2023.
- [4] NXCALS documentation. <https://nxcals-docs.web.cern.ch/current/>.
- [5] P Grafström. Lifetime, cross-sections and activation. <https://cds.cern.ch/record/1047067/files/p213.pdf>.
- [6] CERN. From atomic to nuclear clocks. <https://cerncourier.com/a/from-atomic-to-nuclear-clocks/>.
- [7] Sandro Kraemer et al. Observation of the radiative decay of the 229th nuclear clock isomer. 617(7962):706–710.
- [8] Jochen Ballof. Radioactive molecular beams. <https://cds.cern.ch/record/2797475/files/CERN-THESIS-2021-226.pdf>.